A General Overview for Localizing Short Gamma-Ray Bursts with a CubeSat Mega-Constellation

Fadil Inceoglu [1,2,3], Néstor J. Hernández Marcano [1]*, Rune H. Jacobsen [1] and Christoffer Karoff [4]

[1]Department of Engineering, Aarhus University, Aarhus, Denmark, [2]Cooperative Institute for Research in Environmental Sciences, University of Colorado Boulder, Boulder, CO, United States, [3]National Centers for Environmental Information, National Oceanographic and Atmospheric Administration, Boulder, CO, United States, [4]Department of Geoscience, Aarhus University, Aarhus, Denmark

The gamma-ray burst monitor (GBM) on the *Fermi Gamma-Ray Space Telescope*, for the first time, detected a short gamma ray burst (SGRB) signal that accompanies a gravitational wave signal GW170817 in 2017. The detection and localization of the gravitational wave and gamma-ray source led all other space- and ground-based observatories to measure its kilonova and afterglow across the electromagnetic spectrum, which started a new era in astronomy, the so-called multi-messenger astronomy. Therefore, localizations of short gamma-ray bursts, as counterparts of verified gravitational waves, are of crucial importance since this will allow observatories to measure the kilonovae and afterglows associated with these explosions. Our results show that an automated network of observatories, such as the Stellar Observations Network Group, can be coupled with an interconnected multi-hop array of CubeSats for transients (IMPACT) to localize SGRBs. IMPACT is a mega-constellation of ∼80 CubeSats, each of which is equipped with gamma-ray detectors with ultrahigh temporal resolution to conduct full sky surveys in an energy range of 50–300 keV and downlink the required data promptly for high-accuracy localization of the detected SGRB to a ground station. Additionally, we analyze propagation and transmission delays from receipt of an SGRB signal to ground station offload to consider the effects of constellation design, link, and network parameters such as satellites per plane, data rate, and coding gain from erasure correcting codes among others. IMPACT will provide near–real-time localization of SGRBs with a total delay of ∼5 s and will enable Stellar Observations Network Group telescopes to join the efforts to pursue multi-messenger astronomy and help decipher the underlying physics of these events.

Keywords: multilateration, short gamma-ray bursts, CubeSat, constellation, communication, TDoA

1 INTRODUCTION

The first detection of the gravitational wave (GW) signal from GW150914, which was produced by the mergers of stellar-mass black hole (BH) binaries, by the Laser Interferometer Gravitational Wave Observatory (LIGO) in 2015 (Abbott et al., 2016b), has opened a new era in GW astronomy. The LIGO consists of two observatories located in Hanford Site, WA, and in Livingston, LA, in the United States. The position of the detected GW signal source was calculated using time difference of arrival (TDoA) of the signals at the two detectors, and it was localized to an area of 600 deg^2 in the sky (Abbott et al.,

2016a; Abbott et al., 2016c). Three years after its first detection, LIGO in the United States and Virgo, another observatory in Santo Stefano, Macerata, Italy, observed GW signals from GW170814. This helped the two teams to confine the position of the source to $60 \deg^2$ in the sky because the third observatory provided additional TDoA information (Abbott et al., 2017a).

In addition to the mergers of the stellar-mass BH binaries, the GWs can also be produced by the mergers of neutron star (NS) binaries and NS-BH binaries (Phinney, 1991; Anderson et al., 2008), which are the most promising candidates for generating electromagnetic counterparts to the GWs (Connaughton et al., 2016). These electromagnetic counterparts, which involve NSs, are proposed to be short gamma-ray bursts (SGRBs). The Advanced LIGO and advanced Virgo gravitational wave detectors have observed the first GW signal coming from a NS-NS binary spiraling in toward each other on August 17, 2017. Complementary to the detected GW signals, the gamma-ray burst monitor (GBM) on *Fermi Gamma-Ray Space Telescope* detected a short gamma-ray burst, GRB 170817A, 1.7 s after the coalescence, supporting the first hypothesis of a neutron star merger. These subsequent detections made by GW and gamma-ray observatories provided, for the first time, the direct evidence that merging neutron star binaries generate short gamma-ray bursts and GWs. Fast localization and identification of the electromagnetic counterparts enabled observations of the source across the whole energy spectrum from radio to gamma-ray wavelengths. This joint observational effort, the so-called multi-messenger astronomy, provides insights into astrophysics, dense matter, gravitation, and cosmology (Abbott et al., 2017b).

Gamma-ray bursts (GRBs) are rapid and intense high-energy prompt emissions peaking in the gamma-ray energies (hundreds of keV to MeV), with extended afterglows from radio to X-rays, GeV and even up to TeV gamma rays (D'Avanzo, 2015; Abdalla et al., 2019; Acciari et al., 2019a; Acciari et al., 2019b; Ajello et al., 2019). The durations of the detected GRBs show a bimodal distribution, with local maxima at ~ 0.2 and ~ 20 s and a transition around 2–3 s, indicating two types of GRBs: 1) short gamma-ray bursts (SGRBs) with durations shorter than 2–3 s and 2) long gamma-ray bursts (LGRBs) with durations longer than 2–3 s (Berger, 2014; Shahmoradi and Nemiroff, 2015). Together with their shorter durations, the SGRBs show almost no spectral lags and harder energy spectra compared with the LGRBs (D'Avanzo, 2015). These observational differences suggest that the physical mechanism causing these SGRBs is of different origins than LGRBs. While the majority of nearby LGRBs are associated with core-collapse supernovae, mergers of the compact binaries, such as NS-NS or NS-BH, are proposed as the progenitors of the SGRBs (Berger, 2014; D'Avanzo, 2015).

Following the detection of a potential SGRB candidate, the communications payload of space-based gamma-ray observatories downlinks the data for confirmation and analysis. The communications downlink conveys SGRB descriptive parameters as data packets transmitted through link and networking interfaces, whose end points are the mission control facilities on ground. Given the short time durations of SGRBs, the communications payloads of these missions are designed to ensure a low-latency downlink

between the observatory and mission control to perform follow-up observations. Therefore, communications parameters such as link distance, packet size, and data bit rates, which we refer simply as bit rate from now, are critical in determining the delay performance of a communications payload.

All space-based gamma-ray observatories, such as the *Compton Gamma-Ray Observatory*, the *Fermi Gamma-Ray Space Telescope*, and the *Neil Gehrels Swift Observatory*, are very large and expensive satellite missions. As an emerging alternative platform, CubeSats can provide smaller, cheaper, and faster solutions (Twiggs, 2003). CubeSats arranged in a mega-constellation for global coverage, defined as a large number of CubeSats in various orbital planes that are synchronized and operate together, can increase the field of view (FOV) to the whole sky and therefore can help increase the number of detected SGRBs. Such constellations introduce several communication hops as in the case of a mega-constellation used for detecting SGRBs. Further, they are also equipped with communication payloads fast enough to enable them to convey the potential GRB detection message within time frames similar to those of large and expensive observatory missions.

The message packets consist of sequential groups of bits known as symbols, which define the amplitude, frequency, and phase of the wave signals transmitted. The received signals on ground used to reconstruct the data packets might suffer from absorption, refraction, or dispersion at specific time, which affects the original bits inducing bit errors and making the data packets unusable. To counter this problem, the communications payload uses forward error correction (FEC) (Hamming, 1950), which adds redundant bits that allow to detect and correct erroneous bits previously received. A packet loss, also known as a packet erasure, occurs when a packet arrives with internal errors at the bit level that cannot be corrected even after employing error correcting codes. In this case, the whole packet is discarded, even if some sections of it are useful. A packet loss can also be considered as having occurred when packets do not arrive at all when supposed to. For all these cases, a new type of FEC is implemented above the bits at the packet level known as erasure correcting code. This is achieved by creating redundant packets (instead of redundant bits) as combinations of original ones, which translates in more transmissions utilized to recover when packet losses occur. Thus, erasure correcting codes ensure all data packets are correctly received. However, there is a trade-off between the tolerable delay and the amount of redundant transmissions needed for protection. This depends on the needs of the given mission scenario and is therefore of great interest to search for codes that minimize their introduced redundancy.

Among the alternatives for erasure correcting codes as FEC, block codes such as Reed–Solomon (Reed and Solomon, 1960), low-density parity check (LDPC) (Gallager, 1962), or rate-less codes such as Raptor (Shokrollahi, 2006) could be utilized to cope with packet losses. However, these codes have the drawback of working on a point-to-point basis. This implies that a set of packets needs to be encoded and decoded for every time they are sent between a transmitter and a receiver. Codes based on point-to-point communication incur in delays which are critical for transient applications, given the need of several

hops before reaching the ground system for analysis. For this case, network coding (NC) (Ahlswede et al., 2000), particularly RLNC (Ho et al., 2006), provides an advantage against traditional codes since it does not require to encode and decode on a hop basis. Instead, RLNC sends coded packets as linear combinations of the original set, removing the need to get each individual packet by conveying linearly independent coded packets. This has also the advantage of not acknowledging each single packet, but once the whole set is decodable (Sundararajan et al., 2008). Thus, RLNC-coded packets can be forwarded faster in a potential multi-hop network to reduce the transmission delay when considering packet losses.

Here, we will calculate, using a first-order approach, the average number of CubeSats required in an interconnected multi-hop array of CubeSats for transients (IMPACT) to localize an SGRB with high accuracy and the time it takes for the signal to be transmitted to a ground station on Earth. We assume that each CubeSat in the mega-constellation carries a gamma-ray detector for energy ranges of 50–300 keV, with an effective area between 400 and 600 cm^2 mounted on the largest side surface (20 cm × 30 cm) of the CubeSat. Nanosatellites will orbit the Earth in the low Earth orbit (LEO), which presents the advantage of reduced propagation delays when compared to their medium Earth orbit (MEO) and geostationary orbit (GEO) counterparts.

The SGRBs are most likely associated with GWs, and an accurate and prompt localization of the source of these events will enable us to perform follow-up measurements of the afterglows using an automated network of ground-based observatories such as SONG. As an automated network of observatories, SONG can perform photometric and spectroscopic measurements. The FOV of the SONG telescope is 30″ × 20″, and it is possible to control the telescopes remotely.

In this work, we define a mega-constellation of CubeSats to detect SGRBs, present a discussion about ideal payloads, and analyze the communication parameters for downlinking the data promptly. Our contributions can be listed as follows:

- We review the properties of state-of-the-art scintillation crystals and their readout electronics to ensure we meet the energy range, light yield, decay time, and time resolutions to localize SGRBs with high accuracy.
- We calculate the number of CubeSats required to localize SGRBs with our proposed guidelines, regardless of their origin in space, and for a given accuracy and time uncertainty based on the geometrical properties of the detecting constellation.
- We perform a timing analysis in terms of wave propagation time and data transmission time to observe the effects of the communication system parameters in the event report delay, where we propose RLNC as a suitable erasure correcting code for this mega-constellation (Hernández Marcano and Jacobsen, 2019). Our analysis reveals that the interplay between constellation and communication parameters allows reducing the total communication delay, reaching performance metrics with similar order of magnitude of scientific space missions. We also find that ideal constellation configurations that minimize the total

communication delay for the worst case scenario existing for a given set of parameters. To the best of our knowledge, this is the first time that such analysis is presented.

Our work is organized as follows: **Section 2** describes the CubeSat technology, trends, and prior work regarding detection of SGRBs. In **Section 3**, we present our guidelines for gamma ray detectors, where the localization method is described in **Section 4**. The communications scheme that each CubeSat has to convey the event to ground is presented in **Section 5**. **Section 6** indicates how the constellation is constructed to ensure that we reach a given total number of satellites for the detection requirements. In **Section 7**, we present our analyses and results for the required number of satellites for a given localization accuracy and time delay uncertainty, and the total delay for a given set of communication parameters and different configurations. **Section 8** presents the discussion and conclusions of our work.

2 CUBESATS

A CubeSat, which was developed as a collaborative effort between California Polytechnic State University and Stanford University's Space Systems Development Laboratory in 1999 (Twiggs, 2003), is a standardized model of a miniaturized satellite with a volume of 10 × 10 × 10 cm^3 and a maximum weight of 1.33 kg (1U CubeSat). CubeSat data[1,] since the mid-2000s show that the number of CubeSat missions based on one or several 1U architectures has been increasing, where it showed a sudden jump in 2013. Starting from 2014, most of the CubeSat missions have been mainly on Earth observations and technology demonstrations, while technology demonstration missions have been decreasing since 2013. Scientific missions on the other hand gained momentum in 2017. Major factors in the increase of these types of missions have been the reduction in launch costs and the reliability of spacecraft of subsystem components to space applications.[2,3]

There are several CubeSat missions planned for detection and localization of short- and long-GRBs, former of which can be associated with GW signals, using 5U (Yonetoku et al., 2014) and 6U (Racusin et al., 2017) CubeSat architectures, as well as a swarm of 3U CubeSats (Ohno et al., 2018). To localize the SGRBs accompanying the GWs, Yonetoku et al. (2014) developed Kanazawa-SAT, an X-ray imager based on a coded masked-silicon drift detector, the size of which is 100 cm^2, mounted on a 5U CubeSat. The FOV of the developed X-ray detector is ~1 steradian, and therefore, Yonetoku et al. (2014) suggested to use a fleet of various Kanazawa-SATs to reach whole sky (4π steradians) coverage. On the other hand, Racusin et al. (2017) present BurstCube, a design of a 6U CubeSat carrying four CsI scintillators coupled with arrays of silicon photomultipliers

---

(SiPMs) to complement the bigger missions like *Fermi Gamma-Ray Space Telescope* and Neil Gehrels *Swift* Observatory, but also capable of detecting and localizing the SGRBs. The final proposed configuration of BurstCube includes a constellation of ~10 6U CubeSats to provide whole sky coverage. Ohno et al. (2018) designed CubeSats Applied for MEasuring and LOcalising Transients (CAMELOT), a fleet of 9 3U CubeSats each carrying a CsI(Tl) scintillator coupled with two multi-pixel photon counters (MPPCs) as readout electronics to detect a localize SGRBs. Based on this architecture, Ohno et al. (2018) calculated localization accuracies better than 20′. However, all these prior missions or designs only allow to provide at most coverage when a GRB event occurs in the same hemisphere as the CubeSats' current transit. If this is not the case, then the opportunity for detection and analysis will be lost. Further, even if a GRB event is detected in a given hemisphere, the same as the transit of various CubeSats, but no nearby ground stations exist, then there will be no connectivity possible to provide a low-latency response from detection and reporting.

3 GAMMA-RAY DETECTORS

The most commonly used gamma-ray detectors are made of scintillator detector materials, such as thallium-doped sodium iodide (NaI(Tl)), thallium-doped cesium iodide (CsI(Tl)), and a relatively new cerium-activated lanthanum (III) bromide (LaBr$_3$(Ce)) which provides a higher energy resolution than the previous two (Gilmore, 2008). Prices for a type of a single scintillator[4] are on the order of ~EUR 40,000. Such detector, including readout electronics, is able to fit in a 3U section of a 6U CubeSat, leaving space for other essential subsystems (power supply, communications, on-board computer, etc.). In a scintillation crystal, incoming gamma rays produce primary electrons, which lose their energy by creating secondary electron-hole pairs in the crystal lattice. The created secondary electrons can be found in excited state, which then de-excite by emitting electromagnetic radiation. If this radiation is in, or near, optical wavelengths, it will be detected by a photomultiplier that generates an electrical signal to provide the detector signal. The decay time of the scintillation crystal, which is defined as time it takes for an excited secondary electron to de-excite, must be short to allow high count rates (Gilmore, 2008). Higher counting rates will, in turn, help reduce the uncertainty in detection of timing of an SGRB.

Among the three most common scintillator materials, LaBr$_3$(Ce) provides the shortest decay time of 16 ns (**Table 1**). The decay time depends on the concentration of cerium as an activator in the LaBr$_3$ crystal. This value is crucial as reaching high localization accuracies is correlated with high photon counting rates for a given time interval (bin). Having ultrahigh temporal resolution of gamma-ray detection will increase the photon counting rate and hence provide better counting statistics.

---

[4]Saint Gobain Crystals: https://www.crystals.saint-gobain.com/products/standard-and-enhanced-lanthanum-bromide

TABLE 1 | Properties of most common scintillator materials for gamma-ray detection.

Scintillator	Light yield (Photon/keV)	Decay Time (ns)	Density g cm^{-3}	Refractive Index	Wavelength at Max. Emission (nm)
LaBr$_3$(Ce)[a]	63	16	5.08	~1.9	380
CsI(Tl)[b]	52	1,000	4.51	1.79	550
NaI(Tl)[b]	38	230	3.67	1.85	415

[a]*Data in the related rows are taken from LaBr^3(Ce) data sheet in https://www.crystals.saint-gobain.com*
[b]*Data in the related rows taken from (Gilmore, 2008).*

LaBr$_3$(Ce) has 40 and 17% higher light yield, which is defined as the efficiency in converting ionization energy to light output in the scintillation crystal, compared with NaI(Tl) and CsI(Tl), respectively. LaBr$_3$(Ce) has an inherent radioactive impurity caused by a 0.09% unstable ^{138}La isotope from the default lanthanum, and contamination from its homologue ^{227}Ac (Quarati et al., 2007; Nicolini et al., 2007). However, crystal processing refinements reduced this contamination by a factor of 15 (Quarati et al., 2007). This intrinsic activity of the LaBr$_3$(Ce) crystal is not expected to impact the ultrahigh temporal resolution, although it might increase the background counts (Quarati et al., 2007). LaBr$_3$(Ce) also has a higher efficiency in stopping power due to its higher density (**Table 1**), meaning higher counts in full energy peaks.

In addition to light yield, decay time, and density, refractive index and wavelength at maximum emission are also important features of a scintillator material for choosing the most compatible readout electronics, such as photo-multipliers. Photo-multipliers convert the output of the scintillation crystal, which is a quantity of light, into an electrical signal (Gilmore, 2008). Conventionally, this is achieved by using photomultiplier tubes. Photomultiplier tubes require high biasing voltages, and they are bulky and fragile and sensitive to magnetic fields (Cozzi et al., 2018). SiPMs, on the other hand, are relatively new technology. SiPMs are made of dense arrays of avalanche photodiodes (APDs), and they are insensitive to magnetic fields; they have high multiplication gain (~10^6) and hence negligible electronic noise, low operation voltages, and compact designs, and they provide very high timing resolution in the order of a few nanoseconds (Jenkins, 2015; Cozzi et al., 2018; Butt et al., 2015). In addition to the SiPMs, silicon drift detectors (SDDs) as readout apparatus of scintillators provide high quantum efficiency (>80%) and no photo-multiplication process. However, having no photo-multiplication process makes the system vulnerable to the readout electronic noise (Butt et al., 2015). Although SDDs provide much better spectral resolutions, their drift time, which is defined as the time delay between the time the charge carriers are produced inside the detector and the time that the corresponding current peak at the output is observed, poses a problem, as it is generally in the order of a few microseconds (Butt et al., 2015).

Depending on the main purpose of the gamma-ray detector, the two photo-detectors types could provide different solutions:

1) SiPMs for a higher time-resolution and 2) SDDs for higher spectral resolution (see **Table 1** in (Butt et al., 2015)). Noise contribution due to the dark current in the SiPMs, which is defined as the excess leakage current of a photodiode in reverse bias in the absence of light, is a known issue. However, this issue might be overcome by using SiPMs with small surface areas as dark current scales linearly with their surface area (Bretz et al., 2018) and a coincidence readout method (Ohno et al., 2018). Another known issue is the radiation damage in SiPMs; however, the effects of low-energy photons (≤ 300 keV) are limited to surface damage, instead of the bulk material caused by higher energy photons (Mitchell et al., 2020). Therefore, using SiPMs photo-detectors as readout electronics coupled with a LaBr^3(Ce) scintillator crystal will enable us to obtain a fast response and high temporal resolution, which will in turn help increase the photon counting rates.

In this study, we consider that the design, fit, and volume of our gamma-ray detectors, along with their passive shielding to reduce the effects of scattered gamma-rays, are planned to be in line with the previously proposed missions, such as the BurstCube (Racusin et al., 2017) and CAMELOT (Ohno et al., 2018). This will guide us to avoid exceeding the volume and weight limits and reduce the effects of gamma-ray scattering for our gamma-ray detectors that will be mounted on our planned 6U CubeSats. The effective area of our gamma-ray detectors for the energy range 50–300 keV is planned to be between 400 and 600 cm^2, which could be mounted on the largest side surface (20 cm × 30 cm) of a 6U CubeSat. The large effective area is expected to increase the photon counting rates, and hence improve the counting statistics.
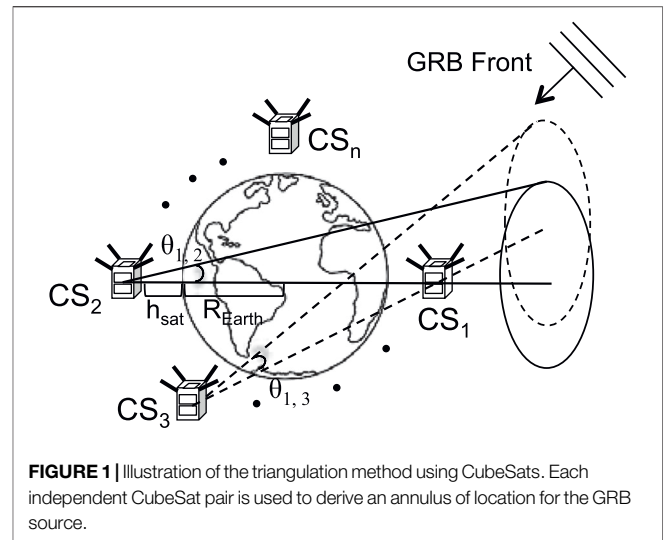
4 TRIANGULATION OF SGRBS

Localization of the GRB sources in space is planned to be achieved by the triangulation method (**Figure 1**). In this method, when a bright GRB occurs in deep space, the photons coming from the source are detected by the first CubeSat (CS$_1$) at time t_1, while they are registered by the second CubeSat (CS^2) at the time t_2.

Assuming that the GRB is a planar wave, meaning that the distance to the source of the event is much larger than the distance between the two CubeSats, the direction of the GRB source can be constrained by the triangulation formula (Predoi et al., 2012; Hurley et al., 2013):

$$\cos\theta_{1,2} = \frac{c\,(t_2 - t_1)}{D_{1,2}} = \frac{c\,\delta t}{D_{1,2}}, \qquad (1)$$

where $\theta_{1,2}$ is the half-angle of the annulus with respect to the vector joining CubeSats 1 and 2, c is the speed of light, $D_{1,2}$ is the distance between the two CubeSats, and δt is the time delay of arrival of the photons between the two CubeSats. A third CubeSat, jointly with the previous two, produces two possible error boxes, causing ambiguity in localization. The ambiguity problem can be overcome by using a fourth CubeSat (or more) in a non-coplanar orbit (Hurley et al., 2013). The finite width of this annulus $d\theta_{1,2}$ and one dimension of the resulting error box $\sigma\,(\theta_{1,2})$

FIGURE 1 | Illustration of the triangulation method using CubeSats. Each independent CubeSat pair is used to derive an annulus of location for the GRB source.

can be calculated by propagating the uncertainty (error) of the time delay in **Eq. 1** as follows (Predoi et al., 2012; Hurley et al., 2013):

$$d\theta_{1,2} = \sigma\left(\theta_{1,2}\right) = \frac{c\,\sigma\,(\delta t)}{D_{1,2}\,\sin\theta_{1,2}}, \qquad (2)$$

where $\sigma\,(\delta t)$ is the uncertainty in the time delay. The radius of each annulus and the right ascension and declination of its center are calculated in a heliocentric frame. The time delay of arrival of the SGRB signal from two satellites δt can be calculated using the cross-correlation method of the observed light curves, which requires precise time synchronizations between the satellites. The uncertainty in the time delay calculations is directly linked to the binning time for count reporting and the photon counting rates, and hence, a gamma-ray detector with a large effective area must be considered to decrease the uncertainties in counting statistics (Ohno et al., 2018). Here, we consider an effective area between 400 and 600 cm^2 for energies ranging from 50 to 300 keV, corresponding to the largest side surface (20 cm × 30 cm) of a 6U CubeSat architecture.

Historically, triangulation for localizations of GRBs has been performed by the interplanetary network (IPN).[5] The 3rd IPN is in operation since the launch of *Ulysses* in 1990[6] and currently consists of *Konus-Wind* in a heliocentric orbit at the L1 point between Earth and Sun (Aptekar et al., 1995), *Mars Odyssey* orbiting Mars (Hurley et al., 2006), the *International Gamma-Ray Laboratory (INTEGRAL)* in GEO (Rau et al., 2005), *Neil Gehrels Swift Observatory* (Gehrels et al., 2004) in LEO, *Fermi* (Meegan et al., 2009) in LEO, and *BepiColombo*, which will arrive in an orbit around Mercury in late 2025.[7] The farthest member of the 3rd IPN is Mars Odyssey that provide a maximum baseline distance of ~ 2.52 AU, when Earth and Mars are the farthest

---

[5]https://heasarc.gsfc.nasa.gov/docs/heasarc/missions/ipn.html

[6]http://www.ssl.berkeley.edu/ipn3/index.html

[7]https://sci.esa.int/web/bepicolombo

apart. This advantage however comes with a cost of a prolonged signal transmission time of about 21 min.

5 SYSTEM OVERVIEW AND DATA TRANSMISSION SCHEME

Performing a fast triangulation of GRBs with mega-constellation of CubeSats in LEO requires defining a distributed multi-hop network, given the limited access time to a CubeSat from ground. Such a constellation allows establishing various paths from the detecting CubeSats to the different ground stations of SONG. In **Figure 2**, we present a system overview of an example path in such network. The path consists of four CubeSats for detection and providing connectivity to a ground station of the SONG ground network. After the GRB front has been detected by a CubeSat, a transmission with descriptive data of the detected light curve event is sent across the path. Then, each CubeSat forwards the data across the network until reaching the ground station belonging to the SONG network. To reach this goal, we consider our transmission scheme in a given established physical network with 1) available energy subsystem budget, 2) radio communications payload in the satellite, 3) access scheme for communication resource (frequency and timeslot) allocation, 4) corresponding network addressing space, and 5) static routing, which we all consider fixed and operative. This ensures each data packet (referred as segment at transport) to be properly routed by a CubeSat and also acknowledged both after transmitted and once successfully received by the ground station. Given that we design our constellations for global coverage, there will always be a connection with the ground station and a path will be established to it. At the end, all the light curve events are gathered in the same facility (e.g., a control room) for data analysis, estimation, and visualization of the relative position

and time of the GRB event through the triangulation method described earlier.

Mega-constellations benefit from shorter round trip times (RTTs) between two neighboring satellites in the network. We define the RTT as the sum of times taken for 1) the propagation of the signal from a transmitting node in the network to a receiving node in a single hop and 2) the propagation of the corresponding acknowledgement signal in the opposite direction. Thus, the RTT for a 580-km LEO orbit that we consider is ~3.87 ms. This is smaller than those in the geostationary orbits, which have RTTs of approximately 240 ms. The shorter RTT of LEO, than medium Earth orbit and geostationary orbit satellite systems, makes LEO satellite networks better in time efficiency when signal transmissions among satellites are considered. Achieving fast and reliable transmission of mission-related data will likely enable near–real-time detection and localization of the SGRBs.

In our proposed system constellation, we consider a reliable data transmission scheme for each hop from a detecting CubeSat to a ground station collocated at SONG. Data transport is based on an end-to-end protocol scheme from a networking perspective, while we consider this in each single possible detection path. However, for our timing analysis, we consider the longest possible time delay occurring when a detection data packet transmission goes through the longest path in the constellation, since all other paths will incur in smaller delays and, thus, will be upper bounded by the delay of the longest path over several hops.

Multi-hop networks, however, might experience segment loss, which in turn affects the performance of the end-to-end protocol scheme (Sundararajan et al., 2011), increasing the total delay, which is critical in our case. A hop-by-hop version of the reliable datagram protocol (RDP) (Velten et al., 1984) is utilized in these types of networks and could reduce this loss. However, RDP establishes a handshake at each hop-pair which will add further
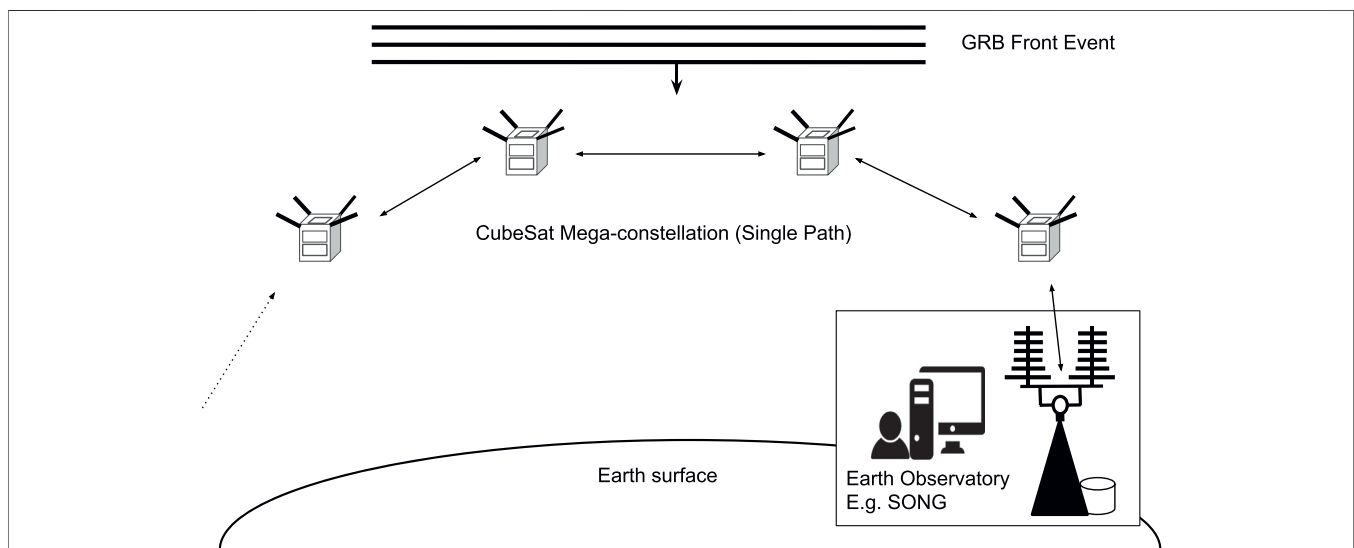

FIGURE 2 | IMPACT system overview of one possible data transmission path in a CubeSat mega-constellation detecting a GRB front from above. The path consists of various detecting and data forwarding CubeSats to an Earth observatory for analysis, for example, a ground station in SONG.

time delays. To minimize the data segment loss rates and the RTT at each hop in the mega-constellation, we use random linear network coding (RLNC) (Ho et al., 2006) at the transport layer, which allows the data segments to be reliably transmitted, despite segment losses (Hernández Marcano and Jacobsen, 2019). This represents the case of FEC in terms of an erasure correcting code at the transport layer. Using RLNC avoids encoding and decoding at each immediate hop, in contrast to the other rate-based or rate-less block codes at the transport layer (Kim et al., 2012). With RLNC, segments are acknowledged as a set on a hop basis removing the caveats of RDP. In this way, RLNC can be regarded as a reliable version of the user datagram protocol (UDP) (Postel, 1980), but without a flow or congestion control mechanism. All these benefits allow RLNC to achieve a lower latency than RDP, which is critical to fetch event reports for analysis.

RLNC achieves these benefits by splitting the transmitted data into blocks of equal size called generations, where each consists of g segments. In each block, coded segments are created as linear combinations of the segments within that block, where the multiplying coding coefficients are drawn from a Galois field (GF) of size q. In RLNC, it is possible to generate recoded segments by recoding previously received coded segments. This process is called coding online or on-the-fly, where decoding coded segments prior to forwarding them to the next hop is not necessary (Sundararajan et al., 2008). To decode a generation, only a linearly independent set of coded segments is necessary and sufficient to recover the original segments. Any coded segment gets appended to its header, a total amount of bits equal to $\alpha = g \log_2(q)$ as overhead to indicate which coding coefficients were used to create them (Heide et al., 2011), which are necessary in the decoding process. In our system, decoding is performed through Gaussian elimination at the final receiver, the ground station, as it possesses the required computation power.

An example of coping with segment losses with RLNC as FEC is shown in **Figure 3**. The vertical lines represent increasing time from top to bottom. At the beginning of the transmission, the leftmost CubeSat starts transmitting coded segments that can be received (solid arrow in **Figure 3**) or lost (solid with cross in

FIGURE 3 | Illustration of the RLNC for the case of two segments and two hops. The vertical lines represent increasing time from top to bottom, and we assume a high field size for the sake of simplicity. The solid arrows represent coded segments, whereas the dashed arrows represent acknowledgements.

Figure 3). Segments are sent continuously until enough linearly independent segments are received, and an acknowledgement is transmitted back for the sending to stop (dashed line). The middle CubeSat starts transmitting toward the CubeSat on the right as soon as segments are received from the previous hop if they are linearly independent. This process is repeated across all hops until the whole message is received at a ground station to decode the data. This is in contrast with any other type of necessary FEC, where all segments would have to be decoded in each hop before being coded and sent to the next introducing more delays.

6 CONSTELLATION DESIGN

To detect and localize SGRBs with high accuracy, we consider using a total number of N_{sat} CubeSats in the LEO for continuous Earth coverage, which are time-synchronized and operate together. An interconnected distributed network of CubeSats in a mega-constellation is therefore composed of P number of planes (polar orbits), each of which accommodates S CubeSats making $P \times S = N_{sat}$, and where various configurations are possible for full sky coverage. This constellation design is classified as Walker type (Walker, 1971). Such polar orbits at 580 km (as the *Fermi Gamma-Ray Space Telescope*) should not affect the sensitivity performance with respect to background, scintillator activation, and SiPM radiation damage, since collision effects from, for example, the inner Van Allen radiation belt, do not appear, yet at this altitude and inclination. As an example, the Complex Orbital Observations Near-Earth of Activity of the Sun - F (CORONAS-F) satellite (Kuznetsov et al., 2002) operated properly in its complete lifetime under similar energy ranges, orbit height, and inclination. The constellation is also designed to ensure that satellites do not collide at the poles. This is reached by allowing relatively small differences in the orbital inclinations and heights without affecting our analysis. From an operational and maintenance perspective, satellites will be deployed similarly to commercial missions, that is, progressively set in orbit in batches, in their planned natural orbits until the final arrangement for start of operations is reached. The satellites in our work do not consider station keeping, nor propulsion systems, and therefore, translation and attitude are determined by natural orbital mechanics. The constituent satellites of the constellation will decay naturally by Earth's gravitational pull and disintegrate on Earth's atmosphere progressively, where replacements will be approached on a failure basis as needed. The total number of satellites depends on a target localization accuracy and available delay uncertainty, which we review in **Section 7**. For a given total number of satellites N_{sat}, we review the different possible configurations of planes and satellites per plane. Based on this, the intra-plane distance, defined as the distance between the CubeSats in the same plane, is given by (Ekici et al., 2001)

$$d_{intra} = (r_E + h) \left[2 \left(1 - \cos\left(2\pi/S\right)\right)\right]^{\frac{1}{2}}, \quad (3)$$

where r_E is the Earth radius and h is the orbit height for all satellites. The orbit height is selected to reach a balance between the total number of satellites and delay. Additionally, the inter-
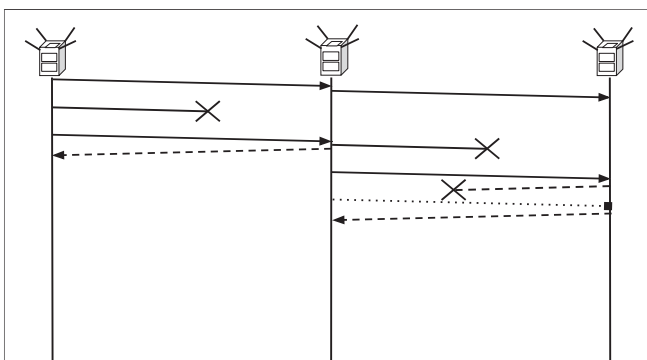
plane distance, which is defined as the distance between CubeSats in adjacent planes, can be calculated following (Ekici et al., 2001):

$$d_{inter} = (r_E + h)[2\,(1 - \cos{(\pi/P)})]^{\frac{1}{2}} \times \cos\phi, \qquad (4)$$

where ϕ is the latitude at which a series of aligned satellites from different planes are located. The distance between a satellite and the ground station, to which the data will be transmitted, is given as follows (Ekici et al., 2001):

$$d_{gnd} = [r_E^2\sin^2\varepsilon_{min} + 2r_Eh + h^2]^{\frac{1}{2}} - r_E\sin\varepsilon_{min}, \qquad (5)$$

where ε_{min} is the minimum elevation angle. The effect of the elevation angle is discussed in **Section 7**. As the orbital planes are assumed to be circular, these distances will be constant throughout the mission lifetime, permitting to define the delay between any given pair of satellites across various hops.

7 ANALYSES AND RESULTS

7.1 Number of CubeSats and Accuracy

In this study, we aim to calculate a number of 6U CubeSats to achieve high-accuracy localization so that SGRBs afterglows can be observed by SONG. The desired localization accuracy for the SGRBs must be much smaller than 20″. To achieve this objective, we assume the following:

- Each CubeSat in a mega-constellation is equipped with gamma-ray detectors for the proposed energy range between 50 and 300 keV, in compliance with the energy range of the nominal BATSE onboard burst trigger (Fishman et al., 1989).
- The accuracy of the detection timing of an SGRB is correlated with the total number of photons counted during its duration. Considering that the median photon fluxes in 50–300 keV energy range for the SGRBs are ~2 photon cm^{-2} s^{-1} (von Kienlin et al., 2020), the effective surface area of the gamma-ray detectors for this energy range must be between 400 and 600 cm^2, corresponding to the side surface of a 6U CubeSat architecture (20 cm × 30 cm). A larger effective surface area will increase the accuracy in detecting the timing of the GRB trigger.
- When an increase in photon counting rates per time bin exceeds 5σ threshold above background, it will be accepted as an SGRB trigger.
- The average number of triggers per year is estimated based on the integral distribution of SGRB fluence in the energy range 50–300 keV [the bottom panel of Figure 10 in von Kienlin et al., 2020]. We calculate the average energy fluence by

$$\overline{\Psi} = \overline{E} \times \int_{t_0}^{t_1} \phi(t)dt, \qquad (6)$$

- where $\overline{E}$ is geometric average of the energies 50 and 300 keV and the integral term is the total photon counts for the

average duration of an SGRB. For SGRBs with photon fluxes larger than 5 photon cm^{-2} s^{-1}, we estimate the average number of SGRB detection as around 20 years^{-1}. As for photon fluxes more than 10 photon cm^{-2} s^{-1}, this rate is around 9 SGRBs year^{-1}.

- The gamma-ray detectors will have time resolutions in the order of μs, which is linked to the readout electronics, to time stamp every photon with its precise arrival time. Higher resolution in time will lead to higher counting rates when time-binning the data leading to reduction of uncertainties in calculated time lags based on cross-correlation.
- We take into account only the statistical error related to δt and neglect uncertainties in distances between each pair of CubeSats, as the main contribution comes from the timing uncertainties (Predoi et al., 2012).
- All of the CubeSats in the mega-constellation must be time-synchronized and their position must be known precisely, which can be achieved with the GPS technology. It was shown that synchronizing a GPS with a CsI scintillation crystal gamma-ray detector and SiPM as a photo-detector is possible, and this setup can provide GPS time stamping of the incoming gamma-ray photons with accuracy and precision better than ~20 μs (Pál et al., 2018).
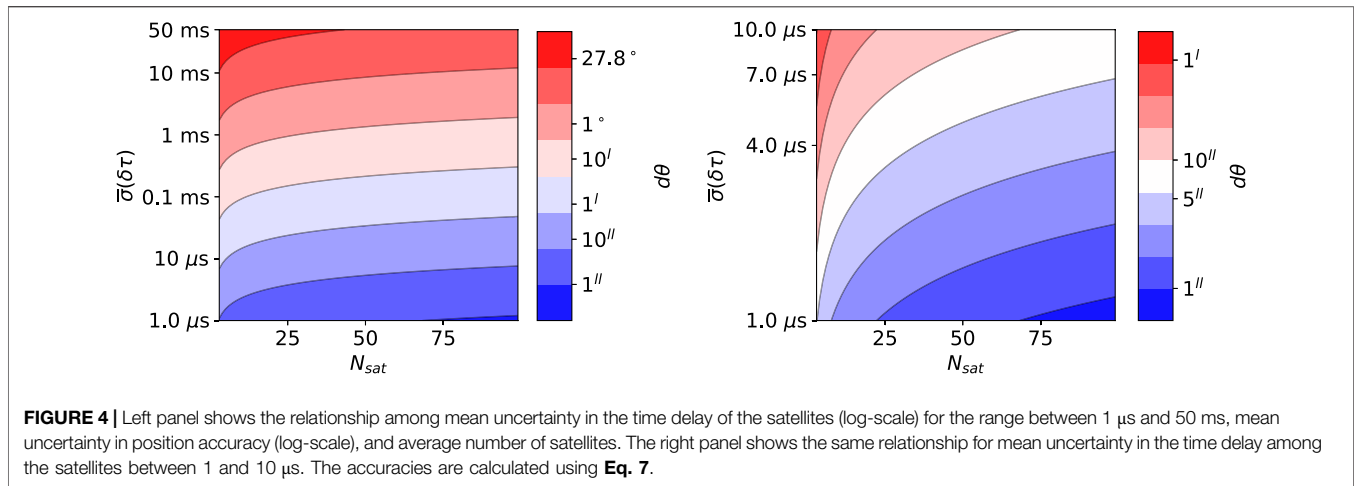
The average localization accuracy for the first-order approximation can therefore be written as

$$d\theta \approx \frac{c}{(r_E + h)}\frac{\overline{\sigma}(\delta t)}{\sqrt{N_{sat} - 1}}, \qquad (7)$$

where $\overline{\sigma}(\delta t)$ is the uncertainty in the average time delay among the paired CubeSats; $(r_E + h)$ represents the average baseline, where r_E is the Earth's radius and h is the orbital altitude; c is the speed of light; and $\sqrt{N_{sat} - 1}$ is the factor that controls the statistical improvement in determining the localization accuracy.

Using **Eq. 7**, we calculated the position accuracies that can be achieved with a given number of satellites, which ranges from 3 to 100 (N_{sat}), and their average time delay accuracies, $\overline{\sigma}(\delta t)$, change between 1 μs and 50 ms. The radius of Earth (r_E) is taken as 6,378.1 km, while the orbital altitude for each satellite is assumed to be 580 km. Satellites at this altitude have orbital lifetimes typically in the order of ~15–20 years (Oltrogge and Leveque, 2011), before being incinerated in Earth's atmosphere due to its gravitational pull and net drag forces.

The results show that position accuracies larger than 1° can be achieved with less than 25 CubeSats (1σ uncertainty from (Hurley et al., 2013)), with an average delay accuracy longer than 1 ms (left panel of **Figure 4**). Reaching accuracies of 1′ requires less than 20 CubeSats, with delay accuracies between around 0.1 ms and 10 μs, or more than 20 CubeSats with delay accuracies around 0.1 ms (left panel of **Figure 4**). To zoom into accuracy range below 1′ to meet the FOV requirement of the SONG telescope, we shortened the average time delay accuracies down to 1–10 μs range and recalculated the relationship between localization accuracies and the number of CubeSats (right panel of **Figure 4**). The results show that around minimum 20 or less CubeSats with time delay accuracy range

FIGURE 4 | Left panel shows the relationship among mean uncertainty in the time delay of the satellites (log-scale) for the range between 1 μs and 50 ms, mean uncertainty in position accuracy (log-scale), and average number of satellites. The right panel shows the same relationship for mean uncertainty in the time delay among the satellites between 1 and 10 μs. The accuracies are calculated using **Eq. 7**.

between 2 and 10 μs provide localization accuracies between around 10″ and 1′, while better accuracies between around 5″ and 1′ require minimum 40 or more CubeSats with average time delay accuracies in the order of a few μs. However, it must be noted that reaching these accuracies is not achievable because of the intrinsic limitation of the SGRB light curves. Although submillisecond variations have been reported previously, it was generally accepted that millisecond variability is the most common feature in the SGRB light curves (Hurley, 2001).

The numbers calculated for the CubeSats in a mega-constellation to achieve high-accuracy localization must also be multiplied by 2 as the half of the CubeSats in the constellation is expected to be in Earth's shadow for a uniformly distributed constellation. This results in ∼80 CubeSats for localization accuracies between a few 10 arcminutes and a few degrees. We must note that reaching these localization accuracies require the uncertainty in the average time delay among the paired CubeSats to be in the order of a few milliseconds.

7.2 Communication Time Delay in Data Transmission

Given the need for reaching a low latency in conveying event reports, we compute the communication time delay of our scenario. The delay for a transmission with acknowledgement during connection for a single path in K number of hops in the network depends on the following:

- We consider a software-configurable binning time of 5 ms for a data point of photon collection and total photon count reporting from readout electronics (Rau et al., 2005). We consider that the light curve of an SGRB extends from 5 s before SGRB peak time to 5 s after it, considering the average SGRB burst duration of 0.2 s (von Kienlin et al., 2020).
- The data point byte representation of a measurement, as shown in **Table 2**, since it will impact on the data segment size. To convey a measurement, we require a time stamp with nanosecond temporal resolution (8 bytes), photon

TABLE 2 | Data point representation.

Variable	Byte size (B)
Time stamp (ns)	8
Photon count value	2
Latitude (degrees)	4
Longitude (degrees)	4
Orbit height (km)	2
Spare	5

count value (2 bytes), latitude in degrees (4 bytes), longitude in degrees (4 bytes), orbit height in km (2 bytes), and spare bytes, in case needed (5 bytes). Thus, a total of 25 bytes are required to represent a single measurement as a data point.

- Based on the previous, we expect to send 2000 data points for the whole curve equivalent to 50 KB of data for a curve. Therefore, if two data points are sent per data segment, 1,000 segments are required, and for six data points, at least 340 segments are needed. Smaller binning times are possible leading to a larger number of segments. Therefore, we also consider a larger number of segments in our results. Therefore, data segment sizes s_d that include 2 data points (50 bytes, referred as 50 B) and six data points (150 bytes, referred as 150 B) will be considered in our analysis.
- The maximum number of satellites to transverse in this type of constellation, which coincides with the maximum number of hops, is $K_{max} = P + \lfloor S/2 \rfloor$ (Yang et al., 2012). In this case, the segments travel across all planes and then one-half inside the final plane to reach a ground station.
- The transmission time costs for data and acknowledgements, which are s_d/R and s_a/R, respectively. s_d, s_a, and R are the data segment size, acknowledgement segment size, and the bit rate, respectively.
- Constant propagation time from forward and return paths, $2t_{p,i}$, where $t_{p,i} = d_i/c$ and $i = 1, \ldots, K$, where d_i are the propagation distances across hops that are intra-plane, inter-plane, and CubeSat to the ground station.

- For each link, we consider working in regime known as propagation dominated, where the bit rate R is larger than a threshold given by $R_{th,i} = (s_d - s_a)/2t_{p,i} \forall i$ (Hernández Marcano and Jacobsen, 2019).

The delay for a transmission with acknowledgement during connection also depends on buffer queueing and internal device processing. However, we did not include these two processes as they are negligible compared to the delays stemming from propagation and transmission processes for small embedded devices (Paramanathan et al., 2014; Hernandez Marcano et al., 2016).

Hence, we calculate the total mean communication delay, which includes both the cost rates for data transmission and the acknowledgements for propagation dominated, separately, based on the following:

$$\mathbb{E}[T_d] = \sum_{i=1}^{K}\left(t_{p,i} + \frac{s_c}{R}\right) + \frac{Ks_c}{R}\mathbb{E}[N_{nf}] \tag{8}$$

$$\mathbb{E}[T_a] = \sum_{i=1}^{K}\left(t_{p,i} + \frac{s_a}{R}\right), \tag{9}$$

where $\mathbb{E}[T_d]$ and $\mathbb{E}[T_a]$ represent delays from the data transmission and the acknowledgements, respectively. We also modify the transmitted segment size as $s_c = s_d + \alpha$ to account for the overhead of the coding coefficients. The delay for RLNC is then given by the sum of the data and acknowledgement delays defined in **Eqs 8** and **9**. The term $\mathbb{E}[N_{nf}]$ in **Eqs 8** and **9** represents the mean number of transmissions of RLNC without acknowledgements in a single path with K hops and is equal to $\mathbb{E}[T_{nf}]/(1\ s)$. $\mathbb{E}[T_{nf}]$ is a unitary delay which is given in (Dikaliotis et al., 2014)

$$\mathbb{E}[T_{nf}](g, K, \epsilon_1, \ldots, \epsilon_K) = \frac{\mathbb{E}[N_w]}{1 - \epsilon_w} + \sum_{i=1, i \neq w}^{K}\frac{\epsilon_w}{\epsilon_w - \epsilon_i}, \tag{10}$$

where $\mathbb{E}[N_w]$ is the mean number of transmissions without losses in the worst hop, ϵ_i is the segment loss rate for each hop, and ϵ_w is the worst segment loss rate in the network. The segment loss rates for each hop are given as $\epsilon_i = 1 - (1 - p_{B,i})^s$, where $i = 1, \ldots, K$, and we consider independent and identically distributed bit errors in a received segment. It must be noted that we ensure that the system operates above an energy-per-bit to spectral noise density threshold for each hop to achieve an operational BER, $p_{B,i}$ in link i. The term $p_{B,i}$ is the bit error rate (BER), defined as the resulting rate of the number of bit errors divided by total bits sent in a transmission on average, and s is the total transmitted segment size in bits for that given link.

We first study the relationship between the total delay and number of segments for data segment sizes of 50 and 150 bytes, and GF sizes of $q = 2$ and $q = 2^8$ (**Figure 5A**). For this calculation, we assume that we have four polar orbital planes, 10 CubeSats in each plane, minimum elevation angle of $\varepsilon_{min} = 0°$, bit rate of $R = 1$ Mbps, and BER $p_{B,i} = p_B = 10^{-5}$ for all links in the constellation. Having 40 CubeSats in four orbital planes is expected to provide localization accuracies between around 10′ and 1°.
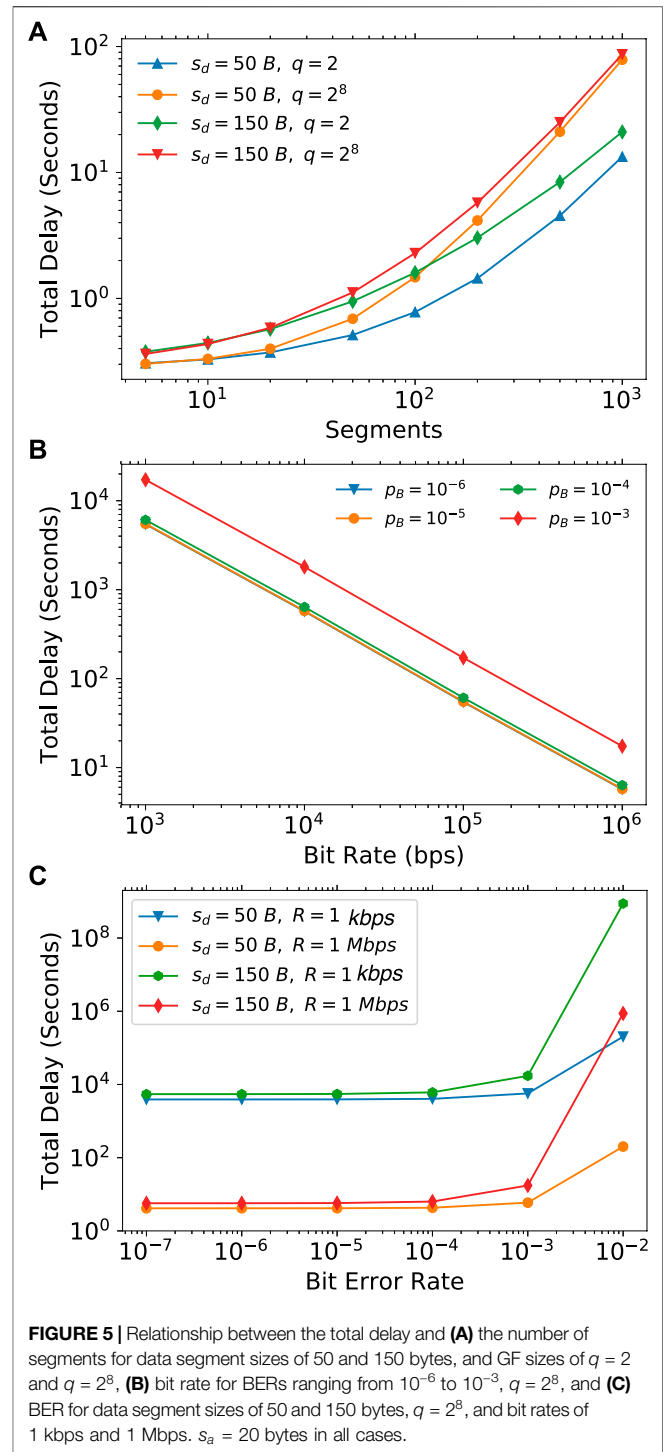
FIGURE 5 | Relationship between the total delay and **(A)** the number of segments for data segment sizes of 50 and 150 bytes, and GF sizes of $q = 2$ and $q = 2^8$, **(B)** bit rate for BERs ranging from 10^{-6} to 10^{-3}, $q = 2^8$, and **(C)** BER for data segment sizes of 50 and 150 bytes, $q = 2^8$, and bit rates of 1 kbps and 1 Mbps. $s_a = 20$ bytes in all cases.

The results show that the total communication delay increases as the number of segments increases for all data segments and GF sizes. Given our current assumptions, for bin sizes as 5 ms, a readout in the order of 10^3 photons would lead 1,000 segments to be sent. This corresponds to the longest total delay of ∼90 s, which is calculated for GF of $q = 2^8$ for the both data segment sizes (red and orange lines in **Figure 5A**), while for larger bin sizes

(as our reference value of 50 ms), the shortest total communication delay of ~2 s would apply for GF of $q = 2$ and data segment size of 50 bytes (blue line in **Figure 5A**). In general, for a large number of segments, the smaller GF size results in shorter total delay, regardless of the data segment sizes for the assumed orbital configuration, because smaller field requires less bits to represent the coding coefficients that are appended to a coded segment. For the case of GF of $q = 2$, only one bit per coding coefficient is necessary to signal it, whereas for GF of $q = 2^8$, one byte per coding coefficient is required that increases the number of bits to be transmitted, and hence the total delay. On the other hand, for a number of segments below 100, the shortest time delay is calculated for the smallest data segment size (blue and orange lines in **Figure 5A**), while the largest data segment size results in longer time delays (red and green lines in **Figure 5A**). Furthermore, for a small number of segments per generation, GF of $q = 2$ results in longer delays than GF of $q = 2^8$. In this case, the major contributing factor for the delay of GF of $q = 2$ is not the coding coefficients, but the frequent transmission of linearly dependent coded segment, particularly at the end of the generation.

Similar to the relationship between total delay and the number of segments, we use four orbital planes accommodating 10 CubeSats in each plane to study the relationship between the bit rates and total delay. Here, we assume that the data segment size is $s_d = 150$ bytes, acknowledgement segment size is $s_a = 20$ bytes, 200 segments to transmit, corresponding to 1,200 data points, if more resolution is needed, and GF of $q = 2^8$. We choose these parameters as a representative example of a bulk transmission of payload data with considerable overhead from the protocol stack to treat bits indistinctly. We changed the BERs from 10^{-6} to 10^{-3} to study the effects of different BERs on the relationship between the total delay and bit rates (**Figure 5B**), since practical BERs for radio links with these applications are in this range.[8] The power law relationship between the bit rates and total delay shows that for higher (lower) bit rates show shorter (longer) delays for all BERs considered, given that the bits are sent into the channel more frequently. The overall levels of the power law relationships are higher for BERs of 10^{-3}, while they are lower with smaller BERs (**Figure 5B**). For BERs 10^{-5} and 10^{-6}, the power law relationship between the bit rates and total delay overlaps. Therefore, target BERs smaller than 10^{-4} do not provide further reductions in the delay.
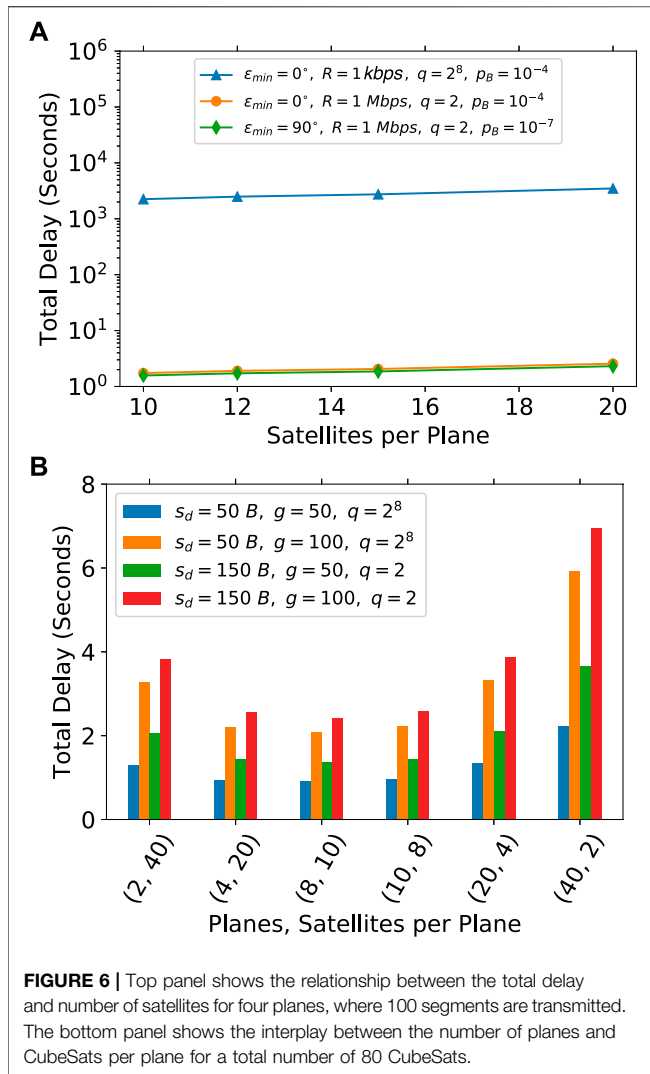
We also calculate the total communication delay for BERs ranging from 10^{-7} to 10^{-2} for the same constellation configuration as in previous calculations. However, this time, we consider four scenarios where the data segment sizes are 50 and 150 bytes, and the bit rates are 1 kbps and 1 Mbps (**Figure 5C**). The results show that smaller bit rates (1 kbps) cause almost 1,000 times longer total delays than the larger bit rates (1 Mbps), regardless of the data segment size. For the bit rate of 1 kbps, larger data segments result in ~1,000 s longer delays than smaller data segments for the BERs ranging from 10^{-7} to around 10^{-4}. For larger BERs of 10^{-2}, the total communication

----
[8] https://gomspace.com/shop/subsystems/communication-(1)/default.aspx

delay for 50 bytes is in the order of ~10^5 s, whereas for 150 bytes goes close to four orders of magnitude higher (blue and green lines in **Figure 5C**), which would be unfeasible in practice. The larger bit rates show the same behavior, where larger data segment size causing longer delays (red and orange lines in **Figure 5C**). Interestingly, for BERs of around 5×10^{-2}, the high bit rates of 1 Mbps with a data segment size of 150 bytes cause longer delay than that by a lower bit rate of 1 kbps with a data segment size of 50 bytes (red and blue lines in **Figure 5C**). This is caused by the relationship of the segment loss rate with the BER and segment size. Therefore, at moderate segment loss rates and fixed BERs, the segment size plays an important role in controlling the total delay. Thus, we consider that data rates on the order of kbps should not be used for communications, where data rates in the order of Mbps provide relatively good results.

We compute the total time delay given by the sum **Eqs 8** and **9**, extending from the detection of an SGRB to reception of this signal by a ground station, for a number of satellites in a mega-constellation of CubeSats, IMPACT. To achieve this, we chose best- and worst-case scenarios. For the best-case scenario, we assumed the elevation angle is 90°, data segment size is $s_d = 50$ bytes, the bit rate is 1 Mbps, GF of $q = 2$, and BER of 10^{-7}. For the worst-case scenario, these parameters are taken as 0°, $s_d = 150$ bytes, the bit rate is 1 kbps, GF of $q = 2^8$, and BER = 10^{-2} (top panel of **Figure 6**). We also include two more realistic scenarios where we fixed the data segment size to $s_d = 150$ bytes, an elevation angle of 0°, and BER of 10^{-4} to achieve more feasible link budgets. The two scenarios include 1) bit rate 1 kbps, GF of $q = 2^8$, and BER of 10^{-4}, and 2) bit rate of 1 Mbps, and GF of $q = 2$. Our scenarios improve the delay bounds for a more realistic setup of the communication parameters since we consider a more practical operational BER. Our best-case scenario is close within a small relative margin to the best scenario achieving a total delay of ~2 s, the only difference being the elevation angle and segment size.

Finally, we investigate on the ideal constellation design parameters for this use case, particularly the number of planes and satellites per plane. To achieve this, we keep fixed the total number of satellites to $N_{sat} = 80$ and vary the number of planes P and satellites per plane S for each of the given set of communication parameters. For all constellations, we fix the elevation angle to 0°, the bit rate to 1 Mbps, and the BER to 10^{-4}, as these are realistic link performance values and orbital configurations to achieve our maximum SGRB localization accuracies between around 10′ and 1°. The orange and green bars in the bottom panel of **Figure 6** are our ideal transmission schemes, considering the delay of the longest possible established route between a detecting CubeSat in the constellation and a ground station, through a given routing protocol. In practice, we exclude the case of one plane since it leads to ambiguity in localization of the SGRBs. We observe that an ideal set of orbital parameters for an orbital altitude of 580 km exist for all transmission schemes which is eight planes and 10 satellites per plane. We also notice that the ideal orbital configuration is independent of the total amount of data to be delivered and the communication parameters utilized. However, this minimum will

FIGURE 6 | Top panel shows the relationship between the total delay and number of satellites for four planes, where 100 segments are transmitted. The bottom panel shows the interplay between the number of planes and CubeSats per plane for a total number of 80 CubeSats.

be sensitive to the BER, and bit rate assumptions on the intra-and inter-satellite links and the downlink to a ground station since the associated delay costs would change as well.

8 DISCUSSION AND CONCLUSIONS

After the detection of the GW signals in 2015 (Abbott et al., 2016b), and the later detection of a short gamma-ray burst by the Fermi telescope in 2017 after GW from an NS-NS binary (Abbott et al., 2017b), these evidences for the association of SGRBs with GWs started the era of GW astronomy. Therefore, the prompt localization of these phenomena will allow ground- and space-based observatories to observe and analyze faster source afterglows that will provide insights into astrophysics, dense matter, gravitation, and cosmology (Abbott et al., 2017b).

In this study, we calculate the number of CubeSats in a mega-constellation to achieve localization accuracies between around 5″ and 1″. As complementary missions to the bigger space-based

gamma-ray observatories, CubeSats can provide smaller, cheaper, and solutions with faster deployment times. The overarching idea is to have a fully coupled, automated localization and observation system, which relies on a CubeSat mega-constellation for prompt localization; and on the Stellar Observations Network Group (SONG) telescope FOV, which is 30″ × 20″. As an automated network of observatories, the SONG telescope can perform photometric and spectroscopic measurements of the afterglows.

In triangulation-based localizations, uncertainties in the time delays between each pair of CubeSats are the major contributors for accuracies in localization calculations. This introduces constraints on the selection of gamma-ray detector materials and their readout electronics. The most promising gamma-ray detectors, which can provide minimum uncertainties in time information, are $LaBr_3(Ce)$ scintillators. These provide the shortest decay time of 16 ns (**Table 1**) as well as 40% and 17% higher light yields than NaI(Tl) and CsI(Tl) crystals, respectively. A good choice for readout electronics to $LaBr_3(Ce)$ can be SiPMs, as they are not sensitive to magnetic fields; they have high multiplication gain ($\sim 10^6$), leading to negligible electronic noise, low operation voltages, and compact designs, and they provide very high time resolution in the order of a few nanoseconds (Butt et al., 2015; Jenkins, 2015; Cozzi et al., 2018). An effective area of 400 cm^2 for the energies ranging from 50 to 300 keV for this detector will also provide high counting rates, and hence smaller uncertainties in the detection time.

We calculated that for a first-order approximation, the number of CubeSats in a mega-constellation is ~ 80 for localization accuracies between a few 10 arcminutes and a few degrees and requires uncertainties in average time delays in the order of a few milliseconds. These numbers are calculated for the orbital altitude of 580 km. We also calculated the number of CubeSats for different orbital altitudes, as an increase in the baseline between each detector pairs will in turn increase the localization accuracy. However, for a first-order approximation, small changes in the orbital altitudes of around a ~ 100 km will not affect the average number of satellites.

Additionally, we calculated the total time delay between the reception of the SGRB signal by the CubeSats and reception of the information by a ground station. A mega-constellation of CubeSats in the LEO is a multi-hop network, where we studied various communication aspects as the bit rate, BER, segment size, and erasure correcting code to reduce the delay. To achieve the maximum SGRB localization accuracies between around 5″ and 1″, we keep the total number of satellites of 80 constant and change the number of planes and satellites per plane for each of the given set of communication parameters that are data segment sizes of s_d = 50 bytes and s_d = 150 bytes, acknowledgement size of s_a = 20 bytes, the bit rate of 1 Mbps, and the BER $p_B = 10^{-4}$. The resulting BER is within the range of target BER values for typical communication link design in CubeSat missions.[9] The results showed that for the given set of parameters, eight planes each accommodating 10 satellites provide the shortest delay time of 5 s.

The BATSE detectors on the *Compton Gamma-Ray Observatory* calculated coordinates with an accuracy of $\pm 10°$ with a time delay of 5.5 s (Barthelmy et al., 1994). The Burst Alert Telescope on the Neil Gehrels *Swift* Observatory provides localization accuracies between 1 and 3′, and the position is distributed within around 20 s of the initial detection.[10] Additionally, the GBM on the *Fermi Gamma-Ray Space Telescope* downlinks the burst notification in 5 s.[11] The delay time between the receipt of an SGRB signal and downlinking the data to the ground station for high-accuracy localization for IMPACT is 5 s, excluding ground processing and telescope movement, which is comparable with the bigger and more costly missions.

In conclusion, an interconnected multi-hop array of CubeSats for transients, IMPACT, will enable us to detect, localize, and study the SGRBs as counterparts to GWs in an energy range from 50 to 300 keV. IMPACT is planned to consist maximum 80 CubeSats, which are synchronized with an onboard GPS. These CubeSats are planned to be distributed in eight orbital planes, each of which accommodating 10 CubeSats that carry $LaBr_3(Ce)$ scintillation crystals coupled with SiMPs as gamma-ray detectors. Our calculations suggest that IMPACT will be able to provide localization accuracies between 10 arcminutes and 1°, which requires uncertainties in average time delays in the order of a few milliseconds with 80 CubeSats. This orbital architecture will also provide an all sky coverage (the field of view is 4π steradians). Additionally, the time it takes for IMPACT to detect an SGRB and downlink the required information for localization to a ground station is expected to be around 5 s.

REFERENCES

Abbott, B. P., Abbott, R., Abbott, T. D., Abernathy, M. R., Acernese, F., Ackley, K., et al. (2016a). Localization and broadband follow-up of the gravitational-wave transient GW150914. *Astrophys. J. Lett.* 826, L13. doi:10.3847/2041-8205/826/1/L13

Abbott, B. P., Abbott, R., Abbott, T. D., Abernathy, M. R., Acernese, F., Ackley, K., et al. (2016b). Observation of gravitational waves from a binary black hole merger. *Phys. Rev. Lett.* 116, 061102. doi:10.1103/PhysRevLett.116.061102

Abbott, B. P., Abbott, R., Abbott, T. D., Abernathy, M. R., Acernese, F., Ackley, K., et al. (2016c). Properties of the binary black hole merger GW150914. *Phys. Rev. Lett.* 116, 241102. doi:10.1103/PhysRevLett.116.241102

Abbott, B. P., Abbott, R., Abbott, T. D., Acernese, F., Ackley, K., Adams, C., et al. (2017a). GW170814: a three-detector observation of gravitational waves from a binary black hole coalescence. *Phys. Rev. Lett.* 119, 141101. doi:10.1103/PhysRevLett.119.141101

Abbott, B. P., Abbott, R., Abbott, T. D., Acernese, F., Ackley, K., Adams, C., et al. (2017b). GW170817: observation of gravitational waves from a binary neutron star inspiral. *Phys. Rev. Lett.* 119, 161101. doi:10.1103/PhysRevLett.119.161101

Abdalla, H., Adam, R., Aharonian, F., Ait Benkhali, F., Angüner, E. O., Arakawa, M., et al. (2019). A very-high-energy component deep in the γ-ray burst afterglow. *Nature* 575, 464–467. doi:10.1038/s41586-019-1743-9

Acciari, V. A., Ansoldi, S., Antonelli, L. A., Arbet Engels, A., Baack, D., Babić, A., et al. (2019a). Teraelectronvolt emission from the γ-ray burst GRB 190114C. *Nature* 575, 455–458. doi:10.1038/s41586-019-1750-x

Acciari, V. A., Ansoldi, S., Antonelli, L. A., Engels, A. A., Baack, D., Babić, A., et al. (2019b). Observation of inverse Compton emission from a long γ-ray burst. *Nature* 575, 459–463. doi:10.1038/s41586-019-1754-6

Ahlswede, R., Cai, N., Li, S.-Y., and Yeung, R. W. (2000). Network information flow. *IEEE Trans.* 46, 1204–1216. doi:10.1109/18.850663

DATA AVAILABILITY STATEMENT

The raw data supporting the conclusions of this article will be made available by the authors, without undue reservation.

AUTHOR CONTRIBUTIONS

All authors collaborated in the motivation, conceptual design, methodology, results analysis and conclusions. FI reviewed the State-of-the-Art, SGRB scientific missions, CubeSats missions, detector payload evaluation, trilateration, number of CubeSats calculation, corresponding plotting and results. NH provided the communication payload State-of-the-Art, constellation, communication and erasure code delay evaluation, corresponding plotting and results. FI and NH discussed the results and conclusions with RJ and CK. FI and NH wrote the paper, where RJ and CK contributed on the manuscript providing significant observations to the study, results and conclusions.

FUNDING

Ajello, M., Arimoto, M., Axelsson, M., Baldini, L., Barbiellini, G., Bastieri, D., et al. (2019). A decade of gamma-ray bursts observed by fermi-LAT: the second GRB catalog. *Astrophys. J.* 878, 52. doi:10.3847/1538-4357/ab1d4e

Anderson, M., Hirschmann, E. W., Lehner, L., Liebling, S. L., Motl, P. M., Neilsen, D., et al. (2008). Magnetized neutron-star mergers and gravitational-wave signals. *Phys. Rev. Lett.* 100, 191101. doi:10.1103/PhysRevLett.100.191101

Aptekar, R. L., Frederiks, D. D., Golenetskii, S. V., Ilynskii, V. N., Mazets, E. P., Panov, V. N., et al. (1995). Konus-W gamma-ray burst experiment for the GGS wind spacecraft. *Space Sci. Rev.* 71, 265–272. doi:10.1007/BF00751332

Barthelmy, S. D., Cline, T. L., Gehrels, N., Bialas, T. G., Robbins, M. A., Kuyper, J. R., et al. (1994). Bacodine the real-time batse gamma-ray burst coordinates distribution network. *AIP Conf. Proc.* 307, 643–647. doi:10.1063/1.45819

Berger, E. (2014). Short-duration gamma-ray bursts. *Annu. Rev. Astron. Astrophys.* 52, 43–105. doi:10.1146/annurev-astro-081913-035924

Bretz, T., Engel, R., Hebbeker, T., Kemp, J., Middendorf, L., Peters, C., et al. (2018). An integrated general purpose SiPM based optical module with a high dynamic range. *J. Instrum.* 13, P06001. doi:10.1088/1748-0221/13/06/P06001

Butt, A. D., Donati, S., Cozzi, G., Busca, P., Fiorini, C., Piemonte, C., et al. (2015). "Comparison of sipm and sdd based readouts of 1? labr3:ce scintillator for nuclear physics applications," in 2015 IEEE nuclear science symposium and medical imaging conference (NSS/MIC), San Diego, CA, October 31–November 7, 2015 (IEEE), 1–4.

Connaughton, V., Burns, E., Goldstein, A., Blackburn, L., Briggs, M. S., Zhang, B.-B., et al. (2016). Fermi GBM observations of LIGO gravitational-wave event GW150914. *Astrophys. J. Lett.* 826, L6. doi:10.3847/2041-8205/826/1/L6

Cozzi, G., Busca, P., Carminati, M., Fiorini, C., Montagnani, G. L., Acerbi, F., et al. (2018). High-resolution gamma-ray spectroscopy with a SiPM-based detection module for 1" and 2" LaBr3:Ce readout. *IEEE Trans. Nucl. Sci.* 65, 645–655. doi:10.1109/TNS.2017.2784238

D'Avanzo, P. (2015). Short gamma-ray bursts: a review. *J. High Energ. Astrophy.* 7, 73–80. doi:10.1016/j.jheap.2015.07.002

Dikaliotis, T. K., Dimakis, A. G., Ho, T., and Effros, M. (2014). On the delay advantage of coding in packet erasure networks. *IEEE Trans. Inf. Theor.* 60, 2868–2883. doi:10.1109/TIT.2014.2306817

Ekici, E., Akyildiz, I. F., and Bender, M. D. (2001). A distributed routing algorithm for datagram traffic in leo satellite networks. *IEEE/ACM Trans. Netw.* 9, 137–147. doi:10.1109/90.917071

Fishman, G. J., Meegan, C. A., Wilson, R. B., Parnell, T. A., Paciesas, W. S., Pendleton, G. N., et al. (1989). "The BATSE experiment on the Gamma Ray Observatory: solar flare hard X ray and gamma-ray capabilities," in *Max' 91 Workshop 2: developments in observations and theory for solar cycle 22*. Editors R. M. Winglee and B. R. Dennis

Gallager, R. (1962). Low-density parity-check codes. *IEEE Trans. Inf. Theor.* 8, 21–28. doi:10.1109/TIT.1962.1057683

Gehrels, N., Chincarini, G., Giommi, P., Mason, K. O., Nousek, J. A., Wells, A. A., et al. (2004). TheSwiftGamma-ray burst mission. *Astrophys. J.* 611, 1005–1020. doi:10.1086/422091

Gilmore, G. R. (2008). *Practical gamma-ray spectrometry*. 2nd Edn. Weinheim, Germany: Wiley-VCH Verlag.

Hamming, R. W. (1950). Error detecting and error correcting codes. *Bell Syst. Tech.* 29, 147–160. doi:10.1002/j.1538-7305.1950.tb00463.x

Heide, J., Pedersen, M. V., Fitzek, F. H. P., and Medard, M. (2011). "On code parameters and coding vector representation for practical RLNC," in 2011 IEEE International Conference on Communications (ICC), Kyoto, Japan, June 5–9, 2011, (IEEE), 1–5.

Hernández Marcano, N. J., and Jacobsen, R. H. (2019). "On the delay advantages of a network coded transport layer in iot nanosatellite constellations,"in ICC 2019 - 2019 IEEE International Conference on Communications (ICC), Shanghai, China, May 20–24, 2019, (IEEE).

Hernandez Marcano, N. J., Sørensen, C. W., Guerrero, J. A. C., Wunderlich, S., Lucani Rötter, D., et al. (2016). On goodput and energy measurements of network coding schemes in the raspberry pi. *J. Electronics* 5 (4), 66. doi:10.3390/electronics5040066

Ho, T., Médard, M., Koetter, R., Karger, D. R., Effros, M., Shi, J., et al. (2006). A random linear network coding approach to multicast. *IEEE Trans. Inf. Theory* 52, 4413–4430. doi:10.1109/tit.2006.881746

Hurley, K., Mitrofanov, I., Kozyrev, A., Litvak, M., Grinkov, A. S. V., Charyshnikov, S., et al. (2006). Mars Odyssey joins the third interplanetary network. *Astrophys. J. Suppl.* 164, 124–129. doi:10.1086/501352

Hurley, K., Pal'shin, V. D., Aptekar, R. L., Golenetskii, S. V., Frederiks, D. D., Mazets, E. P., et al. (2013). The interplanetary network supplement to the Fermi GBM catalog of cosmic gamma-ray bursts. *Astrophys. J. Supp.* 207, 39. doi:10.1088/0067-0049/207/2/39

Hurley, K. (2001). "Some recent, interesting observations of gamma-ray bursts," in *Gamma-ray bursts in the afterglow era*. Editors E. Costa, F. Frontera, and J. Hjorth (Berlin, Heidelberg: Springer Berlin Heidelberg), 3–8

Jenkins, D. (2015). Novel scintillators and silicon photomultipliers for nuclear physics and applications. *J. Phy.Conf. Ser.* 620, 1–7. doi:10.1088/1742-6596/620/1/012001

Kim, M., Cloud, J., ParandehGheibi, A., Urbina, L., Fouli, K., Leith, D., et al. (2012). Network coded TCP (CTCP). *arXiv e-prints.*

Kuznetsov, S., Kudela, K., Ryumin, S., and Gotselyuk, Y. (2002). Coronas-f satellite: tasks for study of particle acceleration. *Adv. Space Res.* 30, 1857–1863. doi:10.1016/s0273-1177(02)00462-3

Meegan, C., Lichti, G., Bhat, P. N., Bissaldi, E., Briggs, M. S., Connaughton, V., et al. (2009). The fermi gamma-ray burst monitor. *Astrophys. J.* 702, 791–804. doi:10.1088/0004-637x/702/1/791

Mitchell, L. J., Phlips, B., Johnson, W. N., Johnson-Rambert, M., Kansky, A. N., and Woolf, R. (2020). Radiation damage assessment of sensl sipms. *arXiv e-prints*

Nicolini, R., Camera, F., Blasi, N., Brambilla, S., Bassini, R., Boiano, C., et al. (2007). Investigation of the properties of a 1"x1" LaBr$_3$:Ce scintillator. *Nucl. Instrum. Methods Phys. Res.* 582, 554–561. doi:10.1016/j.nima.2007.08.221

Ohno, M., Werner, N., Pál, A., Řípa, J., Galgóczi, G., Tarcai, N., et al. (2018). "CAMELOT: design and performance verification of the detector concept and localization capability," in Proceedings of the SPIE Astronomical Instrumentation Space Telescopes and Instrumentation 2018: Ultraviolet to Gamma Ray, (SPIE Proceedings), 10699, 1466–1477.

Oltrogge, D., and Leveque, K. (2011). "An evaluation of cubesat orbital decay," in Proceedings of the 25th annual American Institute of Aeronautics and astronautics/Utah state university Conference on small satellites

Pál, A., Mészáros, L., Tarcai, N., Werner, N., Řípa, J., Ohno, M., et al. (2018). Camelot - concept study and early results for onboard data processing and GPS-based timestamping. *arXiv.*

Paramanathan, A., Pahlevani, P., Thorsteinsson, S., Hundeboll, M., Lucani, D. E., and Fitzek, F. H. P. (2014). "Sharing the pi: testbed description and performance evaluation of network coding on the raspberry pi," in 2014 IEEE 79th vehicular technology conference (VTC Spring), Seoul, South Korea, May 18–21, 2014, (IEEE), 1–5.

Phinney, E. S. (1991). The rate of neutron star binary mergers in the universe - minimal predictions for gravity wave detectors. *Astrophys. J. Lett.* 380, L17–L21. doi:10.1086/186163

Postel, J. (1980). User datagram protocol. RFC 768, USA:RFC. doi:10.17487/rfc0768

Predoi, V., and Hurley, K. (2012). Search for gravitational waves associated with the InterPlanetary Network short gamma ray bursts. *J. Phys. Conf. Series.* 363,012034. doi:10.1088/1742-6596/363/1/012034

Quarati, F., Bos, A. J. J., Brandenburg, S., Dathy, C., Dorenbos, P., Kraft, S., et al. (2007). X-ray and gamma-ray response of a 2"x2" LaBr$_3$:Ce scintillation detector. *Nucl. Instrum. Methods Phys. Res.* 574, 115–120. doi:10.1016/j.nima.2007.01.161

Racusin, J., Perkins, J. S., Briggs, M. S., Georgia, D. N., John, K., Valerie, C., et al. (2017). BurstCube: a CubeSat for gravitational wave counterparts. in *Proceedings of the 227th meeting of the American Astronomical Society*, 147.26

Rau, A., Kienlin, A. V., Hurley, K., and Lichti, G. G. (2005). The 1st INTEGRAL SPI-ACS gamma-ray burst catalogue. *Astron. Astrophys.* 438, 1175–1183. doi:10.1051/0004-6361:20053159

Reed, I., and Solomon, G. (1960). Polynomial codes over certain finite fields. *J. Soc. Ind. Appl. Math.* 8, 300–304. doi:10.1137/0108018

Shahmoradi, A., and Nemiroff, R. J. (2015). Short versus long gamma-ray bursts: a comprehensive study of energetics and prompt gamma-ray correlations. *Mon. Not. Roy. Astron. Soc.* 451, 126–143. doi:10.1093/mnras/stv714

Shokrollahi, A. (2006). Raptor codes. *IEEE Trans. Inf. Theor.* 52, 2551–2567. doi:10.1109/TIT.2006.874390

Sundararajan, J. K., Shah, D., and Medard, M. (2008). "Arq for network coding," in 2008 IEEE international symposium on information theory, Toronto, ON, Canada, July 6–11, 2008, (IEEE), 1651–1655.

Sundararajan, J. K., Shah, D., Medard, M., Jakubczak, S., Mitzenmacher, M., and Barros, J. (2011). Network coding meets tcp: theory and implementation. *Proc. IEEE* 99, 490–512. doi:10.1109/JPROC.2010.2093850

Twiggs, R. (2003). "The next generation of innovative space engineers: university students are now getting a taste of space experience building, launching and operating their own space experiments with low-cost picosatellites," in Proceedings of the 5th ESA international conference on spacecraft guidance, navigation and control systems, (ESA Special Publication), Vol. 516, 409.

Velten, D., Hinden, R., and Sax, J. (1984). "Reliable data protocol. RFC 908, RFC," in *ARPANET Working Group Requests for Comments*. Menlo Park, California: SRI International, 908

von Kienlin, A., Meegan, C. A., Paciesas, W. S., Bhat, P. N., Bissaldi, E., Briggs, M. S., et al. (2020). The fourth fermi-GBM gamma-ray burst catalog: a decade of data. *The Astrophysics Journal* 893, 46. doi:10.3847/1538-4357/ab7a18

Walker, J. G. (1971). Some circular orbit patterns providing continuous whole earth coverage. *J. Br. Interplanet. Soc. (JBIS)* 24, 369–384

Yang, Q., Laurenson, D. I., and Barria, J. A. (2012). On the use of leo satellite constellation for active network management in power distribution networks. *IEEE Trans. Smart Grid* 3, 1371–1381. doi:10.1109/TSG.2012.2197644

Yonetoku, D., Sawano, T., Takata, S., Yoshida1, K., Seta1, H., Toyanago, A., et al. (2014). Establish of gravitational wave astronomy with gamma-ray burst and X-ray transient monitor. *UNISEC Space Takumi J.* 5, 19–27.